



**HAL**  
open science

# pH Sensitive visible or SWIR Quantum Dot Nanoprobes using Conformation- Switchable Copolymeric Ligands

Manon Debayle, Thomas Marchandier, Xiangzhen Xu, Nicolas Lequeux,  
Thomas Pons

## ► To cite this version:

Manon Debayle, Thomas Marchandier, Xiangzhen Xu, Nicolas Lequeux, Thomas Pons. pH Sensitive visible or SWIR Quantum Dot Nanoprobes using Conformation- Switchable Copolymeric Ligands. ACS Applied Materials & Interfaces, 2019, 11 (28), pp.25008-25016. 10.1021/acsami.9b06194 . hal-02282184

**HAL Id: hal-02282184**

**<https://hal.science/hal-02282184>**

Submitted on 9 Sep 2019

**HAL** is a multi-disciplinary open access archive for the deposit and dissemination of scientific research documents, whether they are published or not. The documents may come from teaching and research institutions in France or abroad, or from public or private research centers.

L'archive ouverte pluridisciplinaire **HAL**, est destinée au dépôt et à la diffusion de documents scientifiques de niveau recherche, publiés ou non, émanant des établissements d'enseignement et de recherche français ou étrangers, des laboratoires publics ou privés.

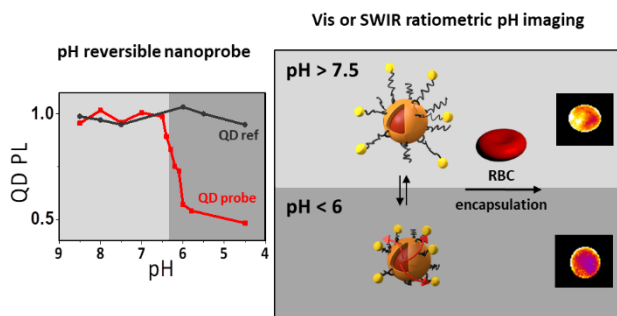


Distributed under a Creative Commons Attribution - NonCommercial - NoDerivatives 4.0 International License

# *pH Sensitive visible or SWIR Quantum Dot Nanoprobes using Conformation-Switchable Copolymeric Ligands*

Manon Debayle,<sup>a</sup> Thomas Marchandier,<sup>a</sup> Xiangzhen Xu,<sup>a</sup> Nicolas Lequeux,<sup>a,\*</sup> Thomas Pons<sup>a,\*</sup>

LPEM, UMR 8213, ESPCI Paris, PSL Research University, CNRS, Sorbonne Université, 75005 Paris, France



**KEYWORDS** quantum dots, biosensors, pH, functional coatings, bionanotechnology, photoluminescence.

**ABSTRACT** Intracellular and extracellular pH are key parameters in many physiological processes and diseases. For example, the extracellular pH of the tumor micro-environment is slightly more acidic than in healthy tissue. *In vivo* mapping of the extracellular pH within the tumor would therefore improve our understanding of the tumor physiology. Fluorescent semiconductor quantum dots (QDs) represent interesting probes for *in vivo* imaging, in particular in the short-wave infrared range (SWIR). Here, pH-sensitive QD nanoprobes are developed using a conformation-switchable surface chemistry. The central fluorescent QD is coated with a copolymer ligand and conjugated to gold nanoparticle quenchers. As the pH decreases from physiological (7.5) to slightly acidic (5.5-6), the copolymer reversibly shrinks, which increases the energy transfer between the QD and the gold quenchers and modulates the QD fluorescence signal. This enables the design of ratiometric QD probes for biological pH ranging emitting in the visible or SWIR range. In addition, these probes can be easily encapsulated and remain functional within ghost erythrocyte membranes, which facilitates their *in vivo* application.

## 1. INTRODUCTION

Fluorescence imaging is a low cost and flexible *in vivo* imaging modality that has become a standard tool for preclinical imaging. In addition to its ease of use, it offers several advantages compared to other imaging techniques such as positron emission tomography or magnetic resonance imaging, including easy multiplexing and the development of

functional probes reporting on their bio-chemical environment. Due to the absorption and scattering of light by superficial tissues, fluorescence signal and spatial resolution decrease however very quickly, and the imaging depth is limited to a few mm. During the past decade, the development of fluorescent imaging in the shortwave infrared range (SWIR), also known as the near infrared (NIR) II range, from 1000 to 1700

nm, have pushed the limits of penetration depth and resolution, thanks to a much lower light scattering compared to the visible or even NIR range. This enables, for example, imaging of the blood vasculature through the skull of mice with ca. 6  $\mu\text{m}$  resolution at nearly 3 mm depth, an unprecedented performance.<sup>1</sup> However, water-soluble SWIR emitting organic fluorophores still lack brightness, with fluorescence quantum yields that usually remain below 1-2 %.

In contrast, fluorescent probes based on quantum dots (QDs) are attracting increasing attention for *in vivo* imaging.<sup>2</sup> These semiconductor nanocrystals display unique optical properties compared to conventional organic fluorophores including high extinction cross sections for linear and multiphoton excitation,<sup>3</sup> high quantum yields, prolonged photostability,<sup>3,4</sup> long fluorescence lifetimes for time-gated detection<sup>5-7</sup>... Most, if not all, QDs share a common basic architecture based on a core-shell semiconductor hetero-structure, typically 2-6 nm in diameter, coated with organic ligands. By changing their size and composition, their emission can be tuned throughout the visible (500-700 nm), near infrared (NIR, 700-1000 nm) and short wave infrared (SWIR, 1000-1500 nm) range.<sup>8,9</sup> With fluorescence quantum yields of 5 to 10 %, SWIR QDs thus appear as promising probes, in particular given the generally poor brightness of other fluorophores in this spectral region.<sup>10-12</sup>

So far most applications of QDs for *in vivo* imaging have consisted in providing contrast to reveal targeted cells or tissues in small animal models, for example using QDs that are bioconjugated to targeting moieties (peptides, antibodies...) via their surface chemistry coating.<sup>13-15</sup> Fewer studies have focused on developing surface chemistry coatings to design QD-based probes that would report on their physico-chemical environment, such as pH, enzymatic activity

or local concentration of specific analytes. pH, for example, is a critical biochemical and physiological parameter. In particular, the pH of the micro-environment of many tumors is slightly more acidic (pH  $\approx$ 5.5-6) than in healthy tissue (pH  $\approx$ 7.4).<sup>16</sup> This acidic pH plays a critical role in many processes such as metabolism, angiogenesis and tumor growth, and may affect drug delivery as well. Developing a SWIR-emitting and pH-sensitive QD for *in vivo* fluorescence imaging would therefore enable mapping the acidity of the tumor micro-environment in depth with a high spatial resolution, as well as monitoring its response to treatments to improve our understanding of these biochemical processes.

Several pH sensitive QD probes have been previously demonstrated, mostly to image endosomal or intracellular pH. For example, QD-dye constructs have been designed where a central visible-emitting QD acts as an antenna for one- or two-photon excitation and is engaged in energy transfer with a pH-sensitive fluorescence dye.<sup>17,18</sup> An alternative strategy relies on ratiometric changes in the fluorescence of large “dot-in-bulk” CdSe/CdS core/shell QDs, where emission from the core provides a reference signal and emission from the large CdS shell is pH-sensitive due to changes in surface passivation.<sup>19</sup> However each of these strategies presents limitations. pH-sensitive organic fluorophores suffer from low photostability. In addition, these probes emit in the visible range, which is of limited use for *in vivo* imaging, and neither of these strategies are easily translatable to the more favorable NIR and SWIR range. Finally, the useful pH range of these probes cannot be easily tuned for optimal response in specific applications. For example, Wang *et al.* recently reported pH sensitive SWIR organic probes, which operate within the pH 2-4 range, far from physiological pH.<sup>20</sup>

Herein, we present a novel strategy to design QD-based pH sensors using a copolymeric coating that

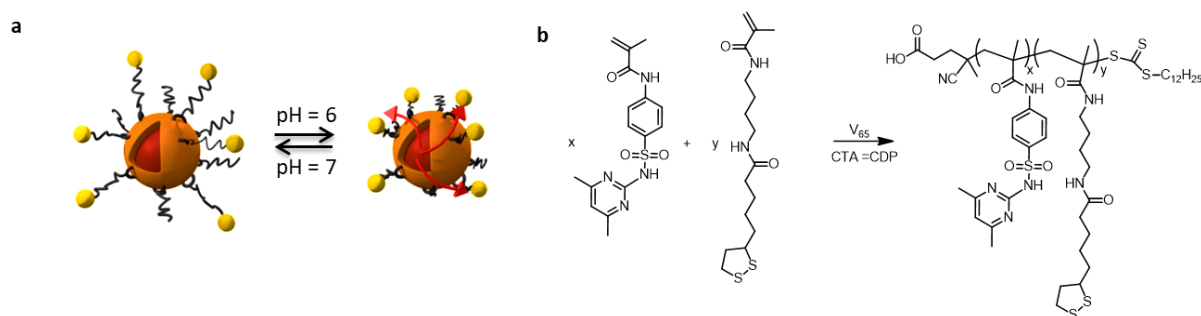


Figure 1. (a) Schematics of the QD-pSMZ/LA-AuNPs nanoprobe in basic (pH 7) or acidic (pH 6) conditions. (b) Synthesis of the SMZ/LA polymers

reversibly changes conformation around a specific pH (Figure 1a). These copolymeric surface ligands are composed of lipoamide and sulfamethazine functions. Lipoamides enable strong binding to the central QD emitter and to small peripheral gold nanoparticle (AuNP) quenchers, while sulfamethazine provides pH-sensitivity by switching reversibly between a charged hydrophilic state and a neutral hydrophobic state around a critical pH value. This transition translates into reversible polymer conformation changes, which modulate the separation distance, and thus the nonradiative energy transfer efficiency, between the QD donor and the AuNP quenchers as a function of pH. This, in turn, modulates the fluorescence signal to provide an optical readout of the environmental pH (Figure 1). Careful design of the pH-sensitive functions and polymer lengths enables us to tune the pH sensitivity range around pH 6-7 under physiological conditions. We characterize the physicochemical and optical response of our QD sensors and demonstrate two strategies to perform ratiometric pH measurements, based on dual color imaging or fluorescence lifetime measurements. We demonstrate that our QD sensors can be easily integrated within erythrocyte ghosts to translate these probes to *in vivo* imaging. Finally, we show that this strategy is adapted to a broad spectral range of QDs, including visible and SWIR emitting QDs, thus paving the way to high resolution fluorescence pH imaging in deep tissues.

## 2. EXPERIMENTAL SECTION

**2.1 Materials:** N-(3-Aminopropyl)methacrylamide hydrochloride (APMA) was purchased from Tebu-bio and 2,2'-Azobis(2,4-dimethyl)valeronitrile from Molekula. All other chemicals were purchased from Sigma-Aldrich and used without further purification.

**2.2 Synthesis of visible-emitting QDs:** Core/shell CdSe/CdS/ZnS nanoparticles were synthesized according to previously published protocols. CdSe cores were synthesized from cadmium myristate and Se powder in octadecene at 240 °C, with reinjections of cadmium oleate and Se dissolved in octadecene at 300 °C to make larger, redder quantum dots if needed.<sup>21</sup> After purification by precipitation in ethanol and resuspension in hexane, a shell composed of typically three monolayers of CdS, two monolayers of CdZnS and two monolayers of ZnS was grown using cadmium oleate, zinc oleate and sulfur precursors in

octadecene, according to the SILAR procedure.<sup>22</sup> The obtained core/shell QDs were precipitated in ethanol and stored in hexane until use. Their concentration was determined using the absorbance of the CdSe cores at 350 nm.<sup>23</sup>

**2.3 Synthesis of SWIR-emitting QDs:** The synthesis of PbS and PbS/CdS QDs was adapted from previous reports.<sup>24,25</sup> Briefly, a sulfur-oleylamine (S-OAm) precursor solution was prepared by heating sulfur (0.16 g) and oleylamine (15 mL) at 125 °C under argon for 30 min. Separately, PbCl<sub>2</sub> (0.834 g) was dissolved in oleylamine (7.5 mL) and degassed under vacuum for 30 min at 125 °C. It was then heated for 30 min at 150 °C under argon atmosphere. The temperature was lowered to 60 °C and the S-OAm solution (2.25 mL) was injected. The temperature was maintained at 60 °C for typically 4-10 min before cooling down to room temperature, depending on the desired final emission wavelength. The PbS QDs were precipitated in ethanol and resuspended in 10 mL hexane. 3 mL of this PbS core solution was precipitated in ethanol and resuspended in octadecene (3 mL). Separately, a mixture of cadmium oleate (3.9 mL, 0.5 M in oleic acid) and octadecene (2.6 mL) was degassed under vacuum at 110 °C then cooled down to 100 °C under argon. The PbS QD solution in octadecene was then injected and maintained at 100 °C for 10 minutes. The solution was then cooled down to room temperature, precipitated in ethanol and resuspended in 10 mL hexane. The core/shell QD concentration was estimated from absorbance and TEM size measurements on the PbS core solution.<sup>26</sup>

**2.4 Synthesis of gold seeds:** Gold seeds nanoparticles, hereafter referred to as AuNP, were synthesized following a previously reported protocol.<sup>27</sup> To a solution of 91 mL of pure milliQ water, NaOH (3 mL, 0.2 M) and then tetrakis(hydroxymethyl)phosphonium chloride (THPC, 24 μL, 80 % wt.) were added. After 5 min of stirring, hydrogen tetrachloroauric acid (HAuCl<sub>4</sub>, 6 mL, 20 mM) was injected in the solution dropwise. The solution turns brown during 15 min of stirring and is stored at 4 °C until used. Their concentration was determined using the extinction cross section of the particles estimated from Mie scattering calculations and their absorbance at 400 nm.<sup>28</sup>

**2.5 Synthesis of pSMZ-LA:** The synthesis of monomers is described in the Supporting Information. The statistic copolymers were prepared by reversible

addition-fragmentation chain transfer (RAFT) polymerization. In those syntheses, we used: 4-cyano-4[(dodecyl-sulfanylthiocarbonyl)sulfanyl]pentanoic acid (CDP) as the chain transfer agent (CTA) and 2,2'-azobis(2,4-dimethylvaleronitrile) (V65) as the initiator. As a typical example, sulfamethazine methacrylamide monomer (3 mmol, 300 eq), dihydrolipoic acid methacrylamide (0.3 mmol, 30 eq), CDP (0.01 mmol, 1 eq) and V65 (0.005 mmol, 0.5 eq) were combined in a 50 mL round-bottomed flask and dissolved in DMF (7 mL). The mixture was purged by argon bubbling for 1 h and thereafter heated in an oil bath at 70°C during 10 h. The polymer was precipitated in methanol, then purified by two cycles of dissolution in DMF and precipitation in methanol and finally dried under vacuum. The polymerization efficiency was evaluated by <sup>1</sup>H NMR, corresponding to a degree of polymerization of approximately DP<sub>n</sub> = 80 and a molar mass M<sub>n</sub> of approx. 29 000 g/mol for this specific example. As a consequence, this polymer will be referred to as pSMZ<sub>65</sub>/LA<sub>15</sub>. Other polymers with different DP<sub>n</sub> and SMZ/LA ratios were prepared in a similar fashion.

**2.6 Ligand Exchange:** The nanoparticles were transferred in aqueous solution after (i) substitution of the initial organic oleate/oleylamine ligands by 3-mercaptopropionic acid (MPA) and then (ii) subsequent MPA ligand exchange with pSMZ/LA statistic copolymers.<sup>29</sup> 4 nmol QDs in hexane were precipitated by ethanol addition followed by centrifugation. QDs were resuspended in pure MPA (400 μL) and left overnight at 60°C. The MPA-modified QDs were thereafter precipitated in chloroform. They were redispersed in dimethylformamide (1 mL) and reprecipitated with potassium tert-butoxide (typ. 50 mg). QDs were centrifuged and the obtained precipitate was rinsed with ethanol and centrifuged again. The 4 nmol of MPA-modified QDs were then resuspended in sodium bicarbonate buffer solution (400 μL, 0.1 M, pH 9). In parallel, 10 mg of the statistic copolymer ligand pSMZ/LA were reduced by sodium borohydride (10-20 mg) in water (2 mL) during 1 h. The ligand and nanoparticle solutions were then mixed together and left to react for one night at 60°C. Then, the polymer exchanged nanoparticles were filtered (100 kDa cut-off Vivaspin membrane) and rinsed with NaCl solution (20 mM, 500 μL, 4 times) to remove excess copolymer and MPA. The resulting nanoparticles were size-purified via ultracentrifugation (268,000 g, 25 min) in a 10-40 wt % sucrose gradient (20 mM

NaCl). The nanoparticle band formed after ultracentrifugation was extracted (BioComp Instruments, Inc., Fredericton, NB, Canada). The excess sucrose was removed by a series of filtration through a Vivaspin 100 kDa membrane. The purified nanoparticles were finally resuspended in buffer solution (1 mL, HEPES/Na 100 mM, NaCl 40 mM, pH 7.5) and stored at 4°C until use. The resulting QDs capped with pSMZ/LA are hereafter referred to as QD-pSMZ/LA.

In addition, QDs insensitive to pH were prepared to provide a reference signal. These QDs underwent a ligand exchange following the same procedure as above with a poly(vinylimidazole-b-sulfobetaine) block copolymer instead of pSMZ/LA. Synthesis of this block copolymer is described in Ref. 29 and in the Supporting Information. The resulting QDs are referred to as SB-QDs.

**2.7 Anchoring gold nanoparticles onto QD-pSMZ/LA:** Quantum Dots coated with pSMZ/LA as described above (1 molar equivalent, typ. 0.5-1 nmol) were dissolved in NaCl solution (1 mL, 150mM) at pH=7.5 and gold nanoparticles (typ. 5 molar equivalents) were added. The solution was left for 10 min, so that the disulfide bridge of LA from the polymer was reduced on AuNP surface allowing the AuNP to be attached onto QD-pSMZ/LA. Then, a short molecular ligand, lipoic acid-sulfobetaine (LASB, see Supporting Information for the description of the synthesis, 1000 equivalents) was added in order to saturate the gold nanoparticles surface. The resulting QD-gold complexes are referred to as QD-SMZ/Au for brevity.

**2.8 Incorporation into erythrocytes:** Erythrocytes were drawn from healthy volunteers and centrifuged in 1 mL saline buffer (HBS: 10 mM HEPES, 150 mM NaCl, pH 7.4) supplemented with 2 mg/mL Na<sub>2</sub>(EDTA) (600 g, 5 min, 3 times). A 20 μL pellet containing erythrocytes was mixed with 60 μL of SMZ/Au- and SB- QDs (typical concentration 80 μM) in hypotonic HEPES saline buffer (HEPES/Na 2.2 mM, NaCl 33 mM, pH 7.5) for 20 minutes. 1 mL of 100% HBS was then added, and erythrocytes were purified by three rounds of centrifugation (14,000 g, 5 min) and resuspension in HBS. In parallel, a solution at 2 mg/mL of amphotericin B5 was prepared and 2 μL and were added to the labeled erythrocytes.

**2.9 Characterization:** Transmission electron microscopy was performed on a Jeol 2010F microscope. Fluorescence spectra were recorded using a F900 spectrometer (Edinburgh Instruments). Fluorescence quantum yields of SWIR emitting QDs were measured by an integrating sphere and confirmed by comparison with a reference indocyanine green dye ( $\Phi = 13\%$  in DMSO). Absorption spectra were recorded using a Shimadzu UV-1800 spectrometer. Fluorescence microscopy images were acquired with a IX71 Olympus wide-field epifluorescence microscope using a  $60 \times 1.2$  NA water immersion objective and a Roper Cascade 512B CCD camera. Dynamic light scattering measurements were performed on an ALV/CGS-3 goniometer system equipped with a HeNe laser (633 nm) and an ALV/LSE-5003 correlator.

### 3. RESULTS AND DISCUSSION

#### 3.1 Copolymer ligand synthesis and characterization

The polymers were synthesized by RAFT copolymerization using 4-cyano-4[(dodecylsulfanylthiocarbonyl)sulfanyl]pentanoic acid (CDP) as the chain transfer agent (CTA) and 2,2'-azobis(2,4-dimethylvaleronitrile) (V65) as the initiator. Polymerizations were carried out at  $70^\circ\text{C}$  in DMF with an initial CTA:initiator ratio of 2:1. The copolymers are composed by two methacrylamide monomers containing sulfamethazine (SMZ) and lipoamide (LA) functions as represented in Figure 1. SMZ is the pH-dependent monomer<sup>30</sup> whereas LA ensures binding of the polymer onto both the central QD emitters and the peripheral AuNP quenchers.  $^1\text{H}$  NMR analysis of the raw polymerization solution and of the purified polymer was used to evaluate the polymerization efficiency (typically  $\approx 40\%$ ) and the SMZ:LA ratio in the purified polymer. As a typical example, we used a SMZ:LA ratio of 5:1, and a CTA:total monomer ratio of 1:180. For this polymer, we estimate a degree of polymerization  $\text{DP}_n = 80$ , (molar mass  $M_n \approx 29000$  g/mol) and a final SMZ:LA ratio of 5:1. As a consequence this polymer will be hereafter referred to as  $\text{pSMZ}_{65}/\text{LA}_{15}$ .

The  $\text{pK}_a$  of sulfonamides can be tuned via chemical modifications, from  $\text{pH} = 5$  to  $\text{pH} = 9$ .<sup>30</sup> In this work, we selected sulfamethazine (SMZ) for its  $\text{pK}_a$  value in the biologically relevant  $\text{pH}$  range, around 7-8. The hydrophilic-hydrophobic transition of the free polymer is observable through turbidity

measurements as a function of  $\text{pH}$ , as shown in Figure 2a. When the  $\text{pH}$  is higher than the polymer cloud point, enough sulfonamide groups are deprotonated and negatively charged to ensure water solubility of the polymer. However, when  $\text{pH}$  is lower than the cloud point, sulfonamide functions become protonated and the predominantly hydrophobic polymer becomes insoluble in water and aggregates. The solution becomes turbid and its transmittance decreases. Figure 2a shows that the cloud point strongly depends on salt concentration in the aqueous solution. Increasing the salt concentration tends to decrease polymer solubility due screening of the electrostatic charges. As a result, the cloud point shifts to higher  $\text{pH}$ , since a larger fraction of SMZ needs to be charged to ensure polymer solubility in water. Interestingly, increasing the polymer size also shifts the cloud point to higher  $\text{pH}$ , from 6 ( $\text{DP}_n = 12$ ) to 8 ( $\text{DP}_n = 100$ ), as shown in Figure 2b. Acid-base titrations show in contrast that the effective  $\text{pK}_a^*$  of the different SMZ polymers were around 7.9 (compared with 7.5 for the SMZ monomer), independently of size or salt concentration. This suggests that larger polymers aggregate more readily than shorter ones, even though they carry the same fraction of charged and uncharged species at a given  $\text{pH}$ . Incorporation of the small fraction of LA functions did not seem to modify the  $\text{pH}$  dependent conformation changes of these polymers.

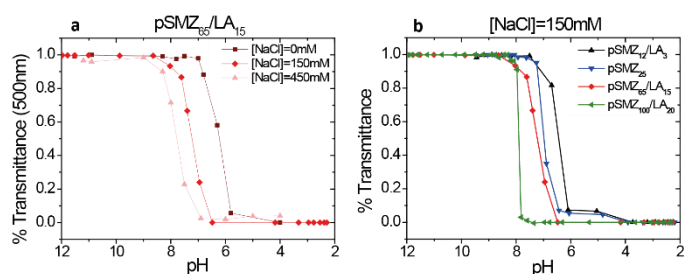


Figure 2. (a) Influence of NaCl concentration on pH-dependent solubility transition of the  $\text{pSMZ}_{65}/\text{LA}_{15}$  polymer. (b) Influence of the polymer length on its pH-dependent solubility transition at  $[\text{NaCl}] = 150$  mM.

#### 3.2 In vitro characterization of the pH-sensitive QD probes

We next investigated the behavior of  $\text{pSMZ}/\text{LA}$  polymers bound to the surface of QDs. Visible emitting CdSe/CdS/ZnS core/multishell QDs were first solubilized in water using mercaptopropionic acid (MPA) as a short labile ligand. A second ligand

exchange was then performed to replace MPA with pSMZ/LA polymers in which lipamides have been previously reduced to dihydrolipoamides (DHLA). QDs were then purified by ultracentrifugation to eliminate MPA and excess polymer ligands. The multiplication of anchoring LA functions on the same polymer strand provides long term stability of the polymer on the QD surface, as previously demonstrated with other poly-LA based polymeric ligands.<sup>31–33</sup> Dynamic light scattering (DLS) measurements in basic pH yield hydrodynamic radii of 8.5–9.5 nm, which is consistent with the expected size of these inorganic QDs (ca. 7 nm in diameter, Figure S1) surrounded by a layer of polymeric ligands.

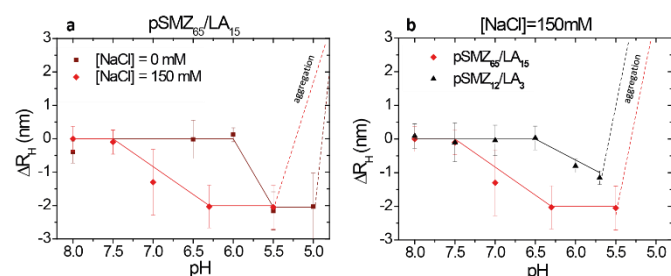


Figure 3. (a) Variation of hydrodynamic radius of QDs coated with pSMZ<sub>65</sub>/LA<sub>15</sub> as a function of the pH for [NaCl] = 0 mM and [NaCl] = 150 mM obtained by DLS measurements (initial hydrodynamic radius at pH 8, 150 mM NaCl: 9.5±0.5 nm; pH 8 without NaCl: 8.5±0.4 nm). (b) Variation of hydrodynamic radius of QDs coated with pSMZ<sub>65</sub>/LA<sub>15</sub> or pSMZ<sub>12</sub>/LA<sub>3</sub> as a function of the pH at [NaCl] = 150 mM (initial hydrodynamic radius of pSMZ<sub>12</sub>/LA<sub>3</sub> coated QDs at pH 8: 6.8±0.4 nm).

Protonation of the SMZ groups at acidic pH leads to a decrease of the hydrodynamic radius of about 2 nm compared to more basic pH (Figure 3a, b). This corresponds to shrinking of the polymer layer surrounding the nanoparticles when it becomes partially hydrophobic. It is important to note that the QDs remain however colloidally stable in water or saline solution, as demonstrated by their monomodal intensity size distribution in DLS. At even more acidic pH, below 5, the polymers become completely hydrophobic, leading to the aggregation of the QDs and to a significant increase of the apparent hydrodynamic radius. Increasing salt concentration and polymer length lead to a shift of the transition pH towards more basic values, consistent with observations on the free polymer. In subsequent

experiments, we select pSMZ<sub>65</sub>/LA<sub>15</sub> with a pH transition around 7 when dispersed in a 150 mM NaCl solution.

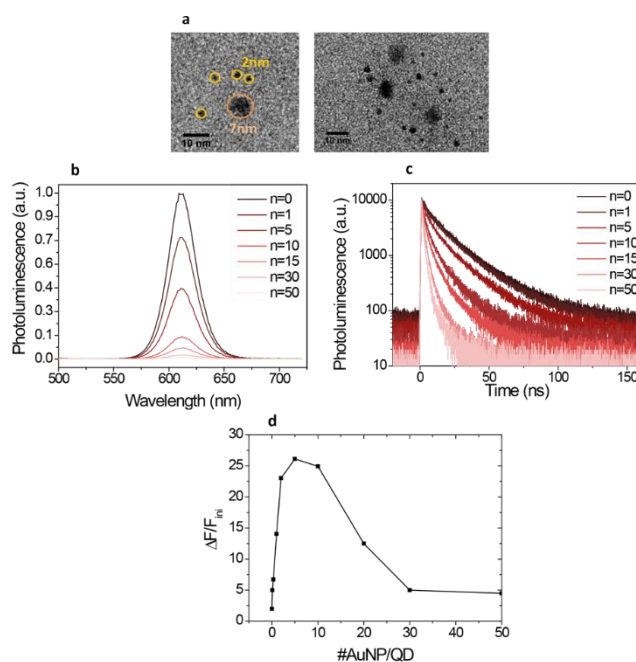


Figure 4: (a) TEM images of the nanoprobe (AuNP:QD = 5). (b) Steady-state and (c) time-resolved photoluminescence of the nanoprobe for different AuNP:QD ratios in basic pH. (d) Relative changes in QD PL at 610 nm between pH 7 and 5.5 normalized by the QD PL at pH 7, as a function of the number of AuNP attached per QD.

AuNPs (ca. 2–3 nm in diameter, Figure S2) were assembled around pSMZ/LA coated QDs using the remaining LA functions that were not immobilized on the QD surface by simply mixing both nanoparticles in basic solution, above the polymer pH transition. Then, a short hydrophilic ligand, lipoic acid-sulfobetaine (LA-SB), was added to saturate the remaining AuNP surface (Figure S11). In its oxidized form, LA-SB is able to bind to the AuNP surface, but not to the QD surface. This prevents displacing the pSMZ/LA polymers from the QDs. Ultrafiltration was then performed to eliminate excess LA-SB and small unconjugated AuNPs. Backtitration shows that, for AuNP:QD ratio below 20, the conjugation of AuNP onto pSMZ/LA QDs reached a >95 % efficiency (Figure S11). This high assembly efficiency could be attributed to the high affinity of free LA functions for AuNPs surfaces. Figure 4a shows electron microscopy pictures of the QD-pSMZ/LA-AuNP assemblies, with central QDs surrounded by several peripheral AuNPs.

Adding increasing numbers of AuNPs around the QDs leads to a progressive quenching of their photoluminescence (PL) intensity, even under basic conditions when the polymer is fully extended, as shown in Figure 4b. In this configuration, 50% quenching efficiency occurs at a AuNP:QD ratio of 5:1. This high quenching efficiency despite the large QD-AuNP center-to-center distance is consistent with previous reports of QD-AuNP nonradiative energy transfer.<sup>34-37</sup> This interpretation is confirmed by time-resolved PL measurements, which show a progressive acceleration of the QD PL kinetics due to the additional nonradiative decay channels (Figure 4c). Quenching efficiencies derived from steady-state and time-resolved PL measurements are consistent with a progressive homogeneous quenching of the QD population, as opposed to total quenching of a QD population fraction.

When these QD-pSMZ/LA-AuNP nanoassemblies were subjected to an acidic pH below the polymer transition pH, shrinking of the polymer reduced the QD-AuNP distance, which increased the QD PL quenching. Figure 4d shows the relative changes in QD PL between basic (pH=7) and acidic (pH=5.5) conditions as a function of AuNP:QD ratio. This relative pH-induced quenching first increases with increasing AuNP:QD ratio, then reaches a maximum value at ratios around 5-10, in the region where the initial QD PL quenching is around 50%. This is also consistent with a nonradiative energy transfer mechanism since energy transfer theories predict that the 50% quenching point is where the slope of the energy transfer efficiency curve vs. separation distance is the highest.<sup>34-37</sup> Then the relative pH-induced changes decrease, since the QD PL becomes more and more efficiently quenched even under basic conditions.

We note that in the absence of AuNP, pH-induced variations in QD PL are very limited (< 2%). This demonstrates that PL variations in QD-pSMZ/LA-AuNP assemblies are indeed due to pH-induced changes in QD-to-AuNP distances and not to other less controllable parameters such as the degree of QD surface passivation or directly to shrinking of the surrounding polymer layer. In the subsequent experiments, we selected the optimal AuNP:QD of 5.

The pH dependence of the selected nanoprobes, QD-pSMZ/LA-5AuNPs, was studied as a function of pH in 150 mM NaCl conditions to mimic biologically

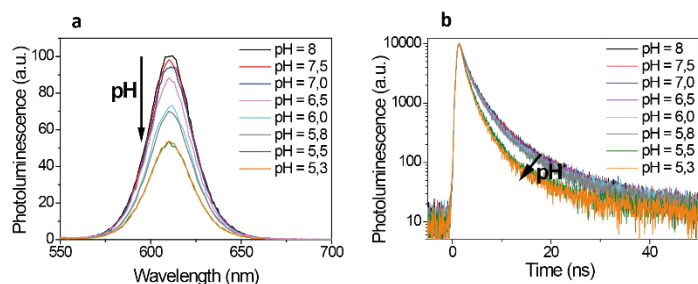


Figure 5. (a) PL spectrum and (b) time-resolved PL of QD-pSMZ-LA-5AuNPs as a function of pH.

relevant salinity. As shown in Figure 5a, the QD PL progressively decreases between pH 7.5 and 5.5, with a more pronounced drop below pH 6.5. The total relative pH-induced variation at pH 5.5 reached about 50%. Time-resolved QD PL accelerates accordingly, as shown in Figure 5b. This progressive quenching is consistent with shrinking of the polymer layer as a progressively more important fraction of SMZ monomers become hydrophobic, while the global nanoprobes assembly remains hydrophilic and colloidal stable in solution.

We then investigate the reversibility of our pH-sensitive nanoprobe. QD-pSMZ/LA-5AuNPs were subjected to several pH-cycles between basic and acidic conditions. Figure 6 and S13 show that pH-induced changes in both PL steady-state intensities and kinetics were reversible for these 3 cycles of pH variations. In contrast, the PL intensity of QD-pSMZ/LA without any conjugated AuNPs remained within +/- 3 % of its initial value when subjected to the same pH cycles. This behavior stems from the fact that pH causes only reversible conformation changes of the polymer layer. This represents a critical advantage over strategies based on pH-cleavable linkers,<sup>38</sup> since those would irreversibly become cleaved over time, even at moderately acidic pH.

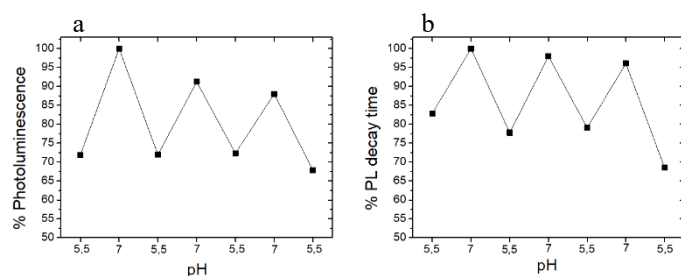


Figure 6: Variations of (a) PL intensity and (b) average PL decay time of QD-pSMZ/LA-5AuNPs over 3 pH cycles between 5.5 and 7.

### 3.3 Ratiometric sensing in erythrocyte carriers

Quantitative pH imaging in biological samples requires a ratiometric signal. Indeed, a weak PL signal could mean either a low QD concentration in a basic or neutral environment or a higher QD concentration in an acidic environment. Variations of PL decay kinetics shown in Figure 5b could enable pH estimations based on lifetime measurements. However these variations occur mainly at pH below 6, whereas QD PL intensities vary more progressively. We therefore chose to develop a dual color system composed of pH-sensitive QD-pSMZ/LA-AuNPs emitting at 610 nm (hereafter referred to as QD610-SMZ/Au) mixed with a reference pH-insensitive QD population coated with a poly(vinylimidazole-b-sulfobetaine) polymer (Figures S8, S9) and emitting at 650 nm (QD650-SB).<sup>29</sup>

Figure 7a shows a strong quenching of QD610-SMZ/Au PL intensity between pH 7 and 5.5 which is consistent with previous measurements. In contrast, the PL intensity of QD650-SB remained constant, providing a useful reference signal. Cycling between neutral and acidic conditions shows that the variations of the 610/650 PL ratio are fully reversible (Figure 7b). Similarly, time-resolved PL measurements shown in Figure 7c demonstrate that the PL decay kinetics of the QD650-SB do not depend on pH within this physiological range, while QD610-SMZ/Au exhibit a

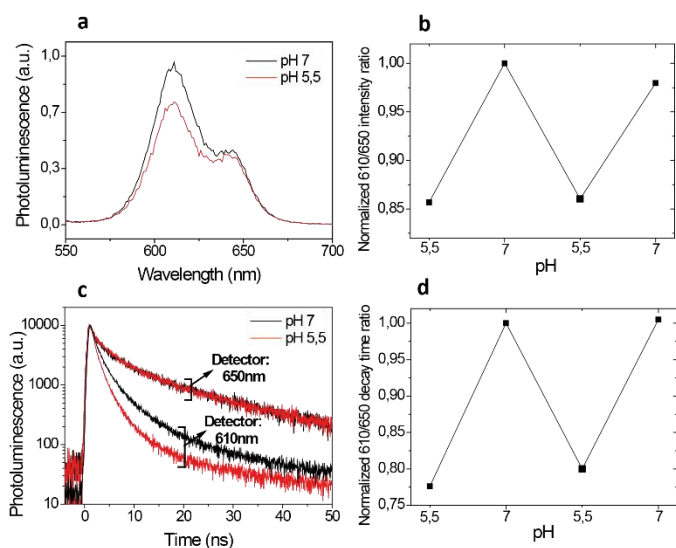


Figure 7: (a) PL spectrum of QD610-SMZ-Au and QD650-SB at pH 7 and 5.5 ([NaCl]=150 mM). (b) Ratio between the PL intensity at 610 nm and 650 nm over 2 cycles of pH variations between 5.5 and 7. (c) Time-resolved PL at 610 and 650 nm at pH 7 and 5.5. (d) Ratio between the average PL decay time at 610 and 650 nm over 2 cycles of pH variations between 5.5 and 7.

marked acceleration under acidic conditions. These changes in PL decay kinetics are also fully reversible when cycling between neutral and acidic conditions. Similar experiments repeated at higher salt concentrations demonstrated a similar behavior, with more pronounced variations of the QD610-SMZ/Au PL properties due to charge screening as discussed above (Figure S14).

Taken together, the above results show that a dual color system composed of QD610-SMZ/Au and QD650-SB could be used to perform ratiometric pH imaging in biological environments. For *in vivo* imaging, two difficulties are however expected. Once injected in the blood stream, the anionic nature of the SMZ polymer is susceptible to induce rapid adsorption of serum proteins. This would lead to subsequent opsonization and efficient uptake by macrophages from the reticuloendothelial system. In addition, two QD populations bearing different surface chemistries may exhibit considerably different biodistributions after intravenous injection, making ratiometric imaging impossible in practice. We propose to circumvent these limitations by incorporating both pH-sensitive and reference QDs into ghost erythrocytes. As the most abundant blood circulating cells, erythrocytes are attractive natural carriers to transport functional imaging agents or drugs in the bloodstream, while ensuring excellent biocompatibility and prolonged blood circulation times.<sup>39</sup> Over the recent years, many different systems based on erythrocyte membranes have been developed, from whole erythrocytes to smaller extruded vesicles and nanoparticle coatings.<sup>39</sup>

Erythrocytes ghosts were loaded with a mixture of QD610-SMZ/Au and QD650-SB using a hypotonic shock, as summarized in Figure 8a.<sup>40</sup> After washing, erythrocytes were modified by incorporating Amphotericin B into their membranes. Amphotericin B enables small ions to cross the erythrocyte membrane barrier, ensuring that the internal pH follows the external pH.<sup>41</sup> The obtained erythrocyte ghosts display heterogeneity in their global QD uptake, due to the different levels of membrane permeability occurring during the hypotonic shock loading procedure. However, the 610/650 PL intensity ratio  $R$  show a monomodal distribution centered around  $R \approx 1.5$  at physiological pH 7.5. In contrast, when the QD-loaded erythrocytes are exposed to a slightly acidic pH of 6 typical of tumor micro-environments, the ratio distribution shifts towards lower values ( $R \approx 1$ ), as shown in Figure 8b, c. This

demonstrates that our dual color ratiometric pH sensor remain functional inside ghost erythrocyte carriers, which opens interesting possibilities for *in vivo* imaging, using either full ghost erythrocytes or smaller extruded vesicles.<sup>39</sup>

emitting at 1100 nm via partial cation exchange,<sup>24,25,44</sup> coated these QDs with a poly(SMZ<sub>12</sub>/LA<sub>3</sub>) ligand, and conjugated these to gold nanoparticles at a 1:4 QD:AuNPs ratio, following the same rationale as for visible emitting QDs. As shown in Figure 9a, the photoluminescence signal of these SWIR emitting QD1100-SMZ/Au nanoprobe dropped below pH 6.5 to about 50 % of its neutral pH intensity. In comparison, the photoluminescence of QD1100-

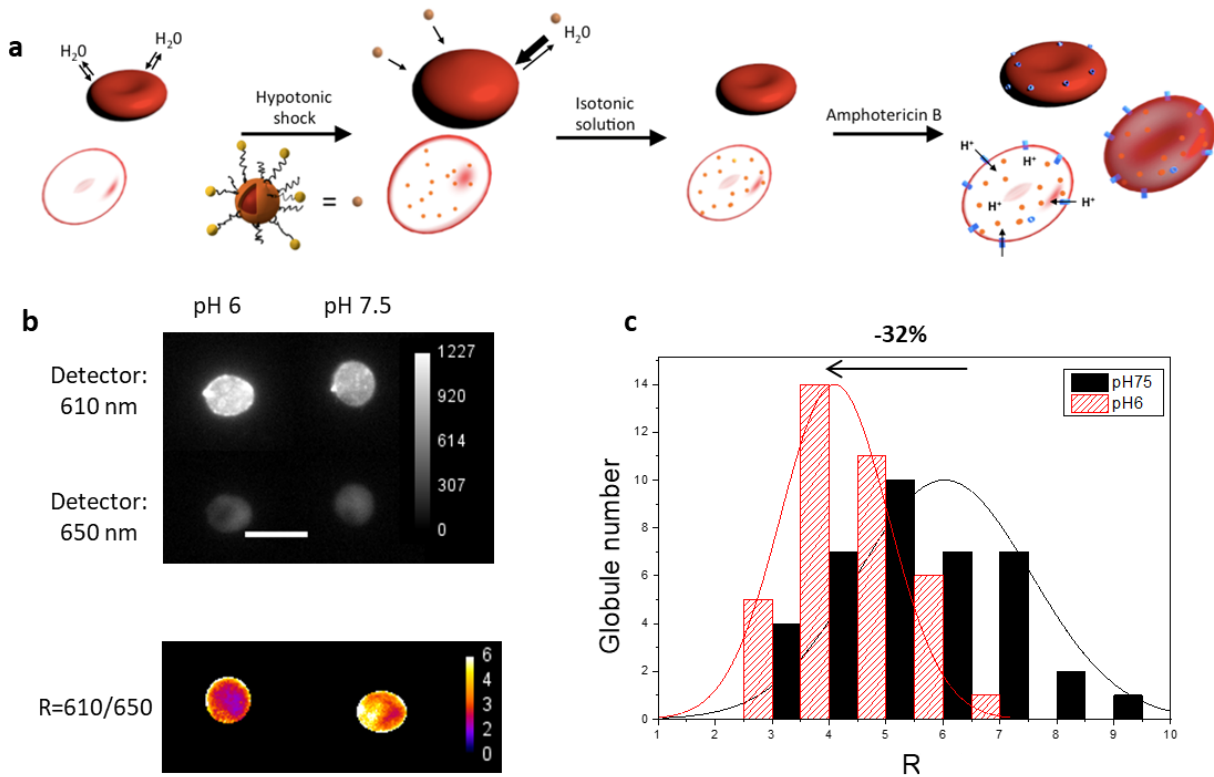


Figure 8. (a) Principles of ghost erythrocyte QD loading and permeabilization with amphotericin. (b) Image of two QD-loaded ghost erythrocytes at 610 nm (top line), 650 nm (medium line) and 610/650 ratiometric image at pH 7.5 (left column) and 6 (right column). Scale bar = 10 μm (c) Distribution histograms of 610/650 intensity ratios among the ghost erythrocyte population at pH 7.5 (black) and 6 (gray).

### 3.4 SWIR emitting pH-sensitive QDs

In our nanoprobe, the pH sensitivity originates from the pH dependent conformational changes of the polymeric surface ligands, and should not depend on the specific nature of fluorescent nanoparticle. In addition, quenching by gold nanoparticles is effective over a broad range of wavelengths.<sup>42</sup> This makes our strategy potentially applicable to fluorescent nanoparticles emitting in other spectral regions. Here we demonstrate pH sensing using PbS/CdS QDs emitting in the SWIR region. This spectral range is particularly interesting for future *in vivo* imaging applications, since it preserves micrometer spatial resolution even several mm deep into the tissue.<sup>43</sup> We synthesized PbS/CdS core/shell quantum dots

SMZ without any attached gold nanoparticles remained constant between pH 8.5 and 4.5 (additional photoluminescence spectra are presented in Figure S16a). This demonstrates that the pH sensitivity of QD1100-SMZ/Au originates from controlled distance changes between the AuNPs and the central QD, due to conformational switching of the polymer coating. Similarly to visible emitting QD-SMZ/Au, these probes showed reversible pH-induced PL changes, over 3 cycles of pH variations between pH=7.5 and pH=6, as shown in Figure 9b and Figure S16b.

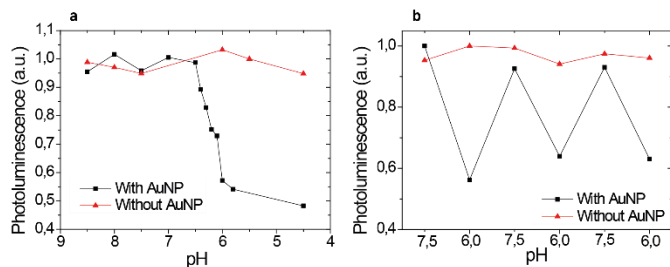


Figure 9. (a) Variations of PL intensity of SWIR ( $\approx 1100$  nm) emitting QD-pSMZ-LA as a function of pH with and without AuNP. (b) Variations of QD PL intensity over 3 pH cycles between 6 and 7.5, with and without AuNP.

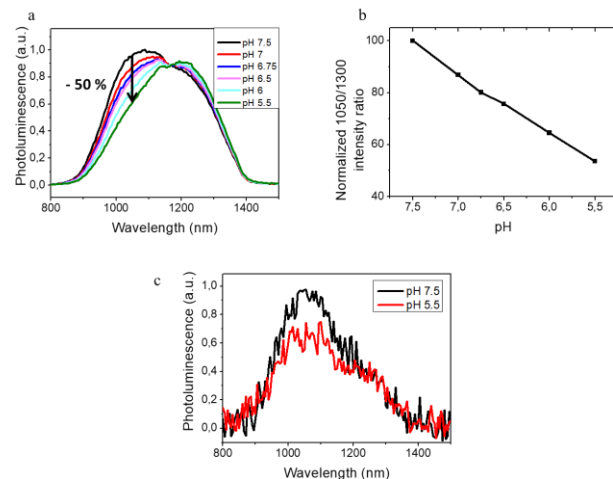


Figure 10. (a) Normalized photoluminescence spectrum of QD1100-SMZ/Au and QD1250-SB as a function of pH. (b) Normalized intensity ratio between 1050 nm and 1300 nm as a function of pH. (c) Photoluminescence spectra of the mixed QD1100-SMZ/Au and QD1250-SB populations incorporated within erythrocytes, at pH 7.5 and 5.5.

We then prepared a mix of two PbS/CdS QD populations: the QD1100-SMZ/Au that is sensitive to pH and QD1250-SB, emitting at around 1250nm and coated with a pH insensitive sulfobetaine polymer coating to provide a spectrally distinct reference signal. Both QD populations have a quantum yield of about 5-6% in saline buffer after functionalization. *In vitro*, the PL intensity of the QD1100-SMZ/Au population drops by about 50% when decreasing the pH from 7.5 to 5.5, compared to the PL intensity of QD1250-SB which remains nearly constant, as shown in Figure 10a. This provides a ratiometric PL signature of the environment pH, as shown in Figure 10b. We then incorporated these two QD populations simultaneously into erythrocyte ghosts and washed the QD-loaded ghosts from free QDs in the solution. The ghosts were then permeabilized to small cations using amphotericin B. The emission spectra of the SWIR QD-loaded erythrocyte ghosts were then recorded in physiological pH (7.5) or slightly acidic pH (5.5). As shown in Figure 10c, the QD1100 / QD1250 nm PL intensity ratio decrease by of about 40% between the two pH environments, similar to their *in vitro* behavior. This demonstrates that ratiometric pH measurements are readily translatable to SWIR-emitting QDs for pH imaging in deep tissues.

#### 4. CONCLUSION

In summary, we have proposed a novel strategy to design environment-sensitive QD nanoprobe, based on reversible conformational changes of surface polymeric ligands. We coated QDs emitting in the visible or SWIR range with pH sensitive copolymer ligands and conjugated them with peripheral gold nanoparticle quenchers. pH-induced switching of the polymer ligand conformation modifies the distance between the QD and gold nanoparticles, resulting in a reversible modulation of the QD photoluminescence. These PL changes occur between physiological pH (7.5) and a more acidic pH (5.5-6), comparable to that encountered in endosomes, tumor microenvironments or inflamed tissues. We demonstrate that these probes enable ratiometric pH measurements, using time-resolved spectroscopy or another population of pH-insensitive reference QDs. Advantages of this strategy includes reversibility over several pH changes cycles, applicability over a large spectral range of QD emission and tunability of the switching pH value via the composition and/or length of the polymer ligands. Furthermore, we demonstrate that our QD nanoprobe can be integrated and are still functional into ghost erythrocytes, opening the way to translating these probes to *in vivo* imaging.

## ASSOCIATED CONTENT

**Supporting Information.** Additional synthesis protocols and characterization.

The following files are available free of charge: Supporting Information (pdf)

## AUTHOR INFORMATION

### Corresponding Author

\*Thomas Pons: thomas.pons@espci.fr; Nicolas Lequeux : nicolas.lequeux@espci.fr

### Author Contributions

The manuscript was written through contributions of all authors. All authors have given approval to the final version of the manuscript.

## ACKNOWLEDGMENT

This work was supported partially by LocalEndoProbes grant CE16-0012 from Agence Nationale de la Recherche. The authors thank the SIMM laboratory for help with DLS measurements.

## REFERENCES

- (1) Hong, G.; Diao, S.; Chang, J.; Antaris, A. L.; Chen, C.; Zhang, B.; Zhao, S.; Atochin, D. N.; Huang, P. L.; Andreasson, K. I.; et al. Through-Skull Fluorescence Imaging of the Brain in a New near-Infrared Window. *Nat. Photonics* **2014**, *8* (9), 723–730. <https://doi.org/10.1038/nphoton.2014.166>.
- (2) Cassette, E.; Helle, M.; Bezdetnaya, L.; Marchal, F.; Dubertret, B.; Pons, T. Design of New Quantum Dot Materials for Deep Tissue Infrared Imaging. *Adv Drug Deliv. Rev.* **2013**, *65*, 719–731.
- (3) Michalet, X.; Pinaud, F. F.; Bentolila, L. a; Tsay, J. M.; Doose, S.; Li, J. J.; Sundaresan, G.; Wu, a M.; Gambhir, S. S.; Weiss, S. Quantum Dots for Live Cells, in Vivo Imaging, and Diagnostics. *Science* **2005**, *307* (5709), 538–544. <https://doi.org/10.1126/science.1104274>.
- (4) Medintz, I. L.; Uyeda, H. T.; Goldman, E. R.; Mattoussi, H. Quantum Dot Bioconjugates for Imaging, Labelling and Sensing. *Nat Mater* **2005**, *4* (6), 435–446. <https://doi.org/nmat1390> [pii]10.1038/nmat1390.
- (5) May, A.; Bhaumik, S.; Gambhir, S. S.; Zhan, C.; Yazdanfar, S. Whole-Body, Real-Time Preclinical Imaging of Quantum Dot Fluorescence with Time-Gated Detection. *J Biomed Opt* **2009**, *14* (6), 60504. <https://doi.org/10.1117/1.3269675>.
- (6) Bouccara, S.; Fragola, A.; Giovanelli, E.; Sitbon, G.; Lequeux, N.; Pons, T.; Lorient, V. Time-Gated Cell Imaging Using Long Lifetime near-Infrared-Emitting Quantum Dots for Autofluorescence Rejection. *J.*

*Biomed. Opt.* **2014**, *19* (5), 051208. <https://doi.org/10.1117/1.JBO.19.5.051208>.

- (7) Pons, T.; Bouccara, S.; Lorient, V.; Lequeux, N.; Pezet, S.; Fragola, A. In Vivo Imaging of Single Tumor Cells in Fast-Flowing Bloodstream Using Near-Infrared Quantum Dots and Time-Gated Imaging. *ACS Nano* **2019**. <https://doi.org/10.1021/acsnano.8b08463>.
- (8) Aharoni, A.; Mokari, T.; Popov, I.; Banin, U. Synthesis of InAs/CdSe/ZnSe Core/Shell1/Shell2 Structures with Bright and Stable near-Infrared Fluorescence. *J. Am. Chem. Soc.* **2006**, *128* (1), 257–264. <https://doi.org/10.1021/ja056326v>.
- (9) Dong, B.; Li, C.; Chen, G.; Zhang, Y.; Zhang, Y.; Deng, M.; Wang, Q. Facile Synthesis of Highly Photoluminescent Ag<sub>2</sub>Se Quantum Dots as a New Fluorescent Probe in the Second Near-Infrared Window for in Vivo Imaging. **2013**.
- (10) Tsukasaki, Y.; Morimatsu, M.; Nishimura, G.; Sakata, T.; Yasuda, H.; Komatsuzaki, A.; Watanabe, T. M.; Jin, T. Synthesis and Optical Properties of Emission-Tunable PbS/CdS Core-shell Quantum Dots for in Vivo Fluorescence Imaging in the Second near-Infrared Window. *RSC Adv.* **2014**, *4* (77), 41164–41171. <https://doi.org/10.1039/C4RA06098A>.
- (11) Benayas, A.; Ren, F.; Carrasco, E.; Marzal, V.; Rosal, B.; Gonfa, B. A.; Juarranz, Á.; Sanz-rodríguez, F.; Jaque, D. PbS / CdS / ZnS Quantum Dots: A Multifunctional Platform for In Vivo Near-Infrared Low-Dose Fluorescence Imaging. **2015**, 6650–6659. <https://doi.org/10.1002/adfm.201502632>.
- (12) Bruns, O. T.; Bischof, T. S.; Harris, D. K.; Franke, D.; Shi, Y.; Riedemann, L.; Bartelt, A.; Jaworski, F. B.; Carr, J. A.; Rowlands, C. J.; et al. Next-Generation in Vivo Optical Imaging with Short-Wave Infrared Quantum Dots. *Nat. Biomed. Eng.* **2017**, *1* (4). <https://doi.org/10.1038/s41551-017-0056>.
- (13) Kim, S.; Lim, Y. T.; Soltesz, E. G.; De Grand, A. M.; Lee, J.; Nakayama, A.; Parker, J. A.; Mihaljevic, T.; Laurence, R. G.; Dor, D. M.; et al. Near-Infrared Fluorescent Type II Quantum Dots for Sentinel Lymph Node Mapping. *Nat Biotechnol* **2004**, *22* (1), 93–97. <https://doi.org/10.1038/nbt920nbt920> [pii].
- (14) Cai, W.; Shin, D.-W.; Chen, K.; Gheysens, O.; Cao, Q.; Wang, S. X.; Gambhir, S. S.; Chen, X. Peptide-Labeled near-Infrared Quantum Dots for Imaging Tumor Vasculature in Living Subjects. *Nano Lett.* **2006**, *6* (4), 669–676. <https://doi.org/10.1021/nl052405t>.
- (15) Smith, B. R.; Cheng, Z.; De, A.; Koh, A. L.; Sinclair, R.; Gambhir, S. S. Real-Time Intravital Imaging of RGD-Quantum Dot Binding to Luminal Endothelium in Mouse Tumor Neovasculature. *Nano Lett.* **2008**, *8* (9), 2599–2606. <https://doi.org/10.1021/nl080141f>.
- (16) Tannock, I. F.; Rotin, D. Acid PH in Tumors and Its

- Potential for Therapeutic Exploitation. *Cancer Res.* **1989**, *49* (16), 4373–4384.
- (17) Preston, T.; Somers, R. C.; Nair, G.; Zimmer, J. P.; Bawendi, M. G.; Nocera, D. G. A Ratiometric CdSe / ZnS Nanocrystal PH Sensor. **2006**, 9–10.
- (18) Dennis, A. M.; Rhee, W. J.; Sotto, D.; Dublin, S. N.; Bao, G. Quantum Dot–Fluorescent Protein FRET Probes for Sensing Intracellular PH. *ACS Nano* **2012**, *6* (4), 2917–2924. <https://doi.org/10.1021/nn2038077>.
- (19) Bruni, F.; Pedrini, J.; Bossio, C.; Santiago-Gonzalez, B.; Meinardi, F.; Bae, W. K.; Klimov, V. I.; Lanzani, G.; Brovelli, S. Two-Color Emitting Colloidal Nanocrystals as Single-Particle Ratiometric Probes of Intracellular PH. *Adv. Funct. Mater.* **2017**, *27* (12), 1–9. <https://doi.org/10.1002/adfm.201605533>.
- (20) Wang, S.; Fan, Y.; Li, D.; Sun, C.; Lei, Z.; Lu, L.; Wang, T.; Zhang, F. Anti-Quenching NIR-II Molecular Fluorophores for in Vivo High-Contrast Imaging and PH Sensing. *Nat. Commun.* **2019**, *10* (1). <https://doi.org/10.1038/s41467-019-09043-x>.
- (21) Yang, Y. A.; Wu, H.; Williams, K. R.; Cao, Y. C. Synthesis of CdSe and CdTe Nanocrystals without Precursor Injection. *Angew. Chem. Int. Ed. Engl.* **2005**, *44* (41), 6712–6715. <https://doi.org/10.1002/anie.200502279>.
- (22) Xie, R.; Kolb, U.; Li, J.; Basché, T.; Mews, A. Synthesis and Characterization of Highly Luminescent CdSe–Core CdS/Zn 0.5 Cd 0.5 S/ZnS Multishell Nanocrystals. *J. Am. Chem. Soc.* **2005**, *127* (20), 7480–7488. <https://doi.org/10.1021/ja042939g>.
- (23) Leatherdale, C. a.; Woo, W.-K.; Mikulec, F. V.; Bawendi, M. G. On the Absorption Cross Section of CdSe Nanocrystal Quantum Dots. *J. Phys. Chem. B* **2002**, *106* (31), 7619–7622. <https://doi.org/10.1021/jp025698c>.
- (24) Cademartiri, L.; Bertolotti, J.; Sapienza, R.; Wiersma, D. S.; Freymann, G. Von; Ozin, G. A. Multigram Scale , Solventless , and Diffusion–Controlled Route to Highly Monodisperse PbS Nanocrystals. **2006**, 671–673.
- (25) Neo, M. S.; Venkatram, N.; Li, G. S.; Chin, W. S.; Ji, W. Synthesis of PbS/CdS Core–Shell QDs and Their Nonlinear Optical Properties. *J. Phys. Chem. C* **2010**, *114* (42), 18037–18044. <https://doi.org/10.1021/jp104311j>.
- (26) Moreels, I.; Lambert, K.; Smeets, D.; De Muynck, D.; Nollet, T.; Martins, J. C.; Vanhaecke, F.; Vantomme, A.; Delerue, C.; Allan, G.; et al. Size-Dependent Optical Properties of Colloidal PbS Quantum Dots. *ACS Nano* **2009**, *3* (10), 3023–3030. <https://doi.org/10.1021/nn900863a>.
- (27) Duff, D. G.; Baiker, A.; Edwards, P. P. A New Hydrosol of Gold Clusters. *J. Chem. Soc. Chem. Commun.* **1993**, 272 (16), 96. <https://doi.org/10.1039/c39930000096>.
- (28) Haiss, W.; Thanh, N. T. K.; Aveyard, J.; Fernig, D. G. Determination of Size and Concentration of Gold Nanoparticles from UV-Vis Spectra. *Anal. Chem.* **2007**, *79* (11), 4215–4221. <https://doi.org/10.1021/ac0702084>.
- (29) Tasso, M.; Giovanelli, E.; Zala, D.; Bouccara, S.; Fragola, A.; Hanafi, M.; Lenkei, Z.; Pons, T.; Lequeux, N. Sulfobetaine-Vinylimidazole Block Copolymers: A Robust Quantum Dot Surface Chemistry Expanding Bioimaging’s Horizons. *ACS Nano* **2015**, *9* (11), 11479–11489. <https://doi.org/10.1021/acsnano.5b05705>.
- (30) Abel, B. A.; Sims, M. B.; McCormick, C. L. Tunable PH- and CO<sub>2</sub>-Responsive Sulfonamide-Containing Polymers by RAFT Polymerization. *Macromolecules* **2015**, *48* (16), 5487–5495. <https://doi.org/10.1021/acs.macromol.5b01453>.
- (31) Yildiz, I.; McCaughan, B.; Cruickshank, S. F.; Callan, J. F.; Raymo, F. M. Biocompatible CdSe–ZnS Core-Shell Quantum Dots Coated with Hydrophilic Polythiols. *Langmuir* **2009**, *25* (12), 7090–7096. <https://doi.org/10.1021/la900148m>.
- (32) Palui, G.; Na, H. Bin; Mattoussi, H. Poly(Ethylene Glycol)-Based Multidentate Oligomers for Biocompatible Semiconductor and Gold Nanocrystals. *Langmuir* **2012**, *28* (5), 2761–2772. <https://doi.org/10.1021/la203968t>.
- (33) Giovanelli, E.; Muro, E.; Sitbon, G.; Hanafi, M.; Pons, T.; Dubertret, B.; Lequeux, N. Highly Enhanced Affinity of Multidentate versus Bidentate Zwitterionic Ligands for Long-Term Quantum Dot Bioimaging. *Langmuir* **2012**, *28* (43), 15177–15184. <https://doi.org/10.1021/la302896x>.
- (34) Yun, C. S.; Javier, a; Jennings, T.; Fisher, M.; Hira, S.; Peterson, S.; Hopkins, B.; Reich, N. O.; Strouse, G. F. Nanometal Surface Energy Transfer in Optical Rulers, Breaking the FRET Barrier. *J. Am. Chem. Soc.* **2005**, *127* (9), 3115–3119. <https://doi.org/10.1021/ja043940i>.
- (35) Pons, T.; Medintz, I. L.; Sapsford, K. E.; Higashiya, S.; Grimes, A. F.; English, D. S.; Mattoussi, H. On the Quenching of Semiconductor Quantum Dot Photoluminescence by Proximal Gold Nanoparticles. *Nano Lett.* **2007**, *7* (10), 3157–3164. <https://doi.org/10.1021/nl071729+>.
- (36) Breshike, C. J.; Riskowski, R. A.; Strouse, F. Leaving Förster Resonance Energy Transfer Behind: Nanometal Surface Energy Transfer Predicts the Size-Enhanced Energy Coupling between a Metal Nanoparticle and an Emitting Dipole. **2013**.
- (37) Hildebrandt, N.; Spillmann, C. M.; Algar, W. R.; Pons, T.; Stewart, M. H.; Oh, E.; Susumu, K.; Sebastian, A. D.; Delehanty, J. B.; Medintz, I. L. Energy Transfer with Semiconductor Quantum Dot Bioconjugates: A Versatile Platform for Biosensing , Energy Harvesting , and Other Developing Applications. **2017**. <https://doi.org/10.1021/acs.chemrev.6b00030>.

- (38) Wang, L.; Fan, Z.; Zhang, J.; Changyi, Y.; Huang, C.; Gu, Y.; Xu, Z.; Tang, Z.; Lu, W.; Wei, X.; et al. Evaluating Tumor Metastatic Potential by Imaging Intratumoral Acidosis via PH-Activatable near-Infrared Fluorescent Probe. *Int. J. Cancer* **2015**, *136* (4), E107–E116. <https://doi.org/10.1002/ijc.29153>.
- (39) Han, X.; Wang, C.; Liu, Z. Red Blood Cells as Smart Delivery Systems. **2018**. <https://doi.org/10.1021/acs.bioconjchem.7b00758>.
- (40) Antonelli, A.; Sfara, C.; Battistelli, S.; Canonico, B.; Arcangeletti, M.; Manuali, E.; Salamida, S.; Papa, S.; Magnani, M. New Strategies to Prolong the In Vivo Life Span of Iron-Based Contrast Agents for MRI. *PLoS One* **2013**, *8* (10), e78542. <https://doi.org/10.1371/journal.pone.0078542>.
- (41) Deuticke, B.; Kim, M.; Zöllner, C. The Influence of Amphotericin B on the Permeability of Mammalian Erythrocytes to Nonelectrolytes, Anions and Cations. *BBA - Biomembr.* **1973**, *318* (3), 345–359. [https://doi.org/10.1016/0005-2736\(73\)90199-5](https://doi.org/10.1016/0005-2736(73)90199-5).
- (42) Riskowski, R. A.; Armstrong, R. E.; Greenbaum, N. L.; Strouse, F. Triangulating Nucleic Acid Conformations Using Multicolor Surface Energy Transfer. **2016**. <https://doi.org/10.1021/acsnano.5b05764>.
- (43) Hong, G.; Diao, S.; Chang, J.; Antaris, A. L.; Chen, C.; Zhang, B.; Zhao, S.; Atochin, D. N.; Huang, P. L.; Andreasson, K. I.; et al. Through-Skull Fluorescence Imaging of the Brain in a New near-Infrared Window. *Nat. Photonics* **2014**, *8* (9), 723–730. <https://doi.org/10.1038/nphoton.2014.166>.
- (44) Pietryga, J. M.; Werder, D. J.; Williams, D. J.; Casson, J. L.; Schaller, R. D.; Klimov, V. I.; Hollingsworth, J. A. Utilizing the Lability of Lead Selenide to Produce Heterostructured Nanocrystals with Bright, Stable Infrared Emission. *J. Am. Chem. Soc.* **2008**, *130* (14), 4879–4885. <https://doi.org/10.1021/ja710437r>.

## SUPPORTING INFORMATION

*pH Sensitive Visible or SWIR Quantum Dot Nanoprobes using Conformation-Switchable Copolymeric Ligands*

*Manon Debayle,<sup>a</sup> Thomas Marchandier,<sup>a</sup> Xiangzhen Xu,<sup>a</sup> Nicolas Lequeux,<sup>a,\*</sup> Thomas Pons<sup>a,\*</sup>*

LPEM, UMR 8213, ESPCI Paris, PSL Research University, CNRS, Sorbonne Université, 75005  
Paris, France

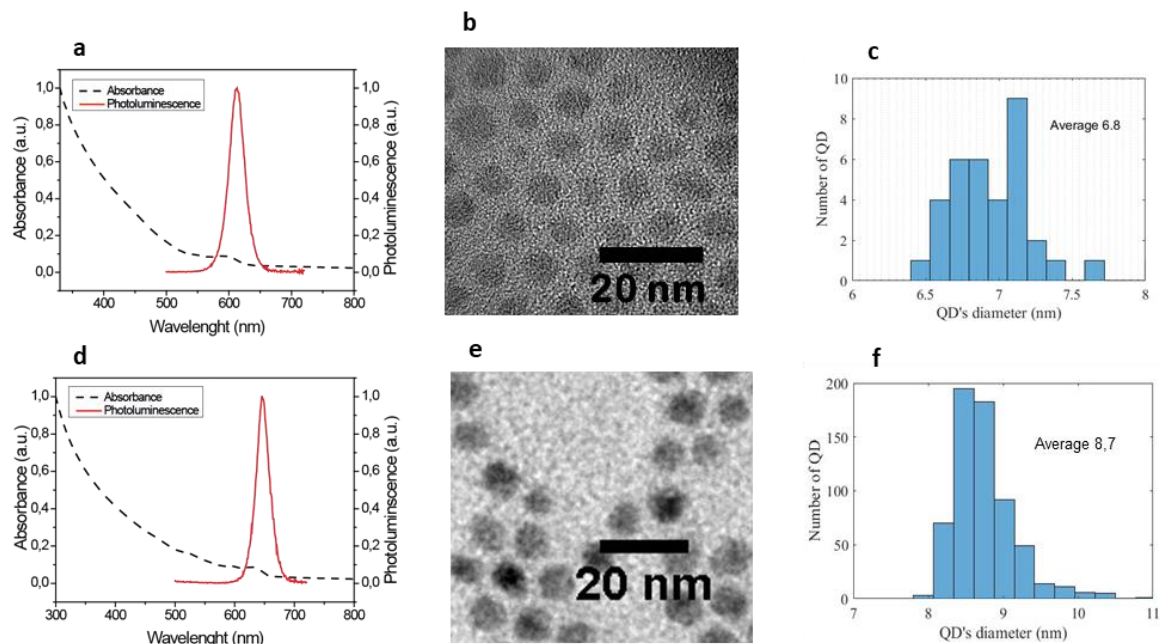


**Figure S1.** (a) Absorption and photoluminescence emission spectra of QD610 in hexane; (b) TEM image of QD610; (c) Size distribution of QD610. (d) Absorption and photo-luminescence emission spectra of QD650 in hexane; (e) TEM image of QD650; (f) Size distribution of QD650.

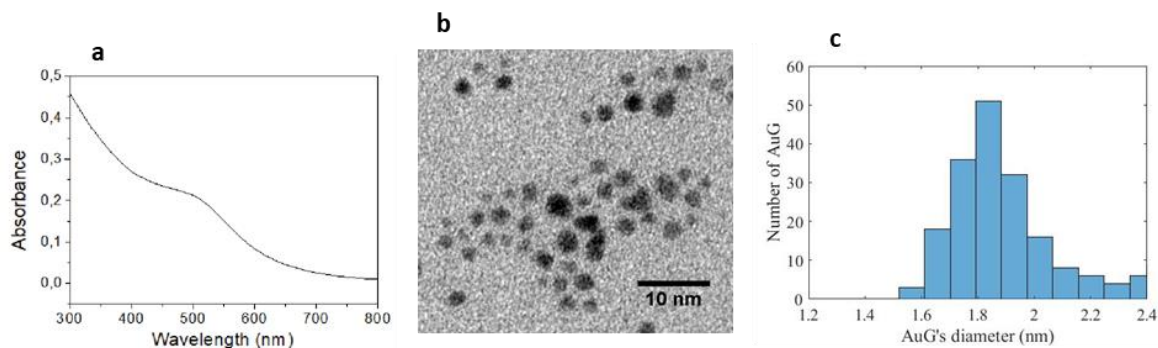


**Figure S2.** (a) Absorption spectra of AuNP in water; (b) TEM image of AuNP; (c) Size distribution of AuNP.

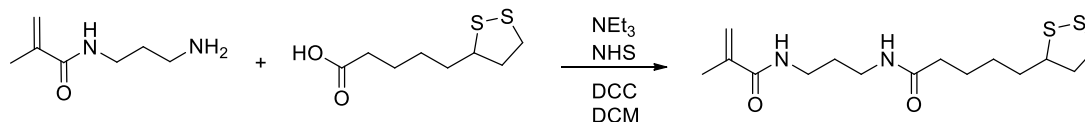


**Figure S3.** Synthesis of the LA monomer

**Synthesis of lipoamide (LA) methacrylamide.** To a suspension of APMA-HCl (2 g, 11.2 mmol) in dichloromethane (20 mL) was added triethylamine (2.5 mL, 17.9 mmol). Methanol (2 mL) was introduced to obtain complete solubilization. A solution of LA (2.76 g, 13.4 mmol) in dichloromethane (5 mL) was then added, followed by NHS (1.58 g, 13.8 mmol) in one portion.

The reaction mixture was cooled down to 0°C with an ice bath and a solution of DCC (3.00 g, 14.4 mmol) in dichloromethane (10 mL) was injected dropwise. The medium was warmed up to room temperature and further stirred overnight. A pale yellow solution containing a white precipitate was obtained. The solution was washed with a 0.1 M aqueous HCl solution (2x50 mL), deionized water (1x50 mL) and a 0.2 M aqueous NaOH solution (2x50 mL). The organic phase was separated, dried over MgSO<sub>4</sub>, filtrated and concentrated under reduced pressure. The crude residue was purified by chromatography on silica (eluent: hexane/ethyl acetate 1/4, then hexane/acetone 1/1) to give DHLA (2.88 g, 8.71 mmol, 78%) as a pale yellow solid.<sup>1</sup> R<sub>f</sub> = 0.37 (hexane/acetone 1/1); <sup>1</sup>H NMR (CDCl<sub>3</sub>, 400 MHz): δ 7.03 (s, 1H); 6.87 (s, 1H); 5.72 (s, 1H); 5.29 (s, 1H); 3.53-3.39 (m, 1H); 3.29-3.20 (m, 4H); 3.14-3.01 (m, 2H); 2.43-2.35 (m, 1H); 2.18 (t, J = 8.0 Hz, 2H); 1.92 (s, 3H); 1.88-1.80 (m, 1H); 1.68-1.55 (m, 6H); 1.48-1.33 (m, 2H).

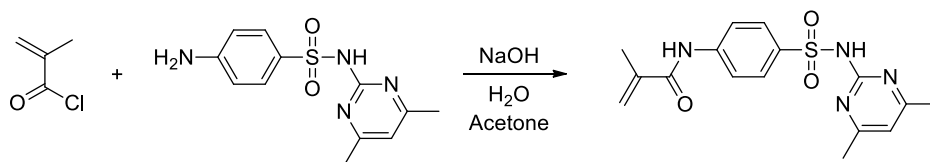


**Figure S4.** Synthesis of the SMZ monomer

**Synthesis of sulfamethazine (SMZ) methacrylamide.** Commercial sulfamethazine (10 mmol) was dissolved in 40 mL of 1:1 mixture of acetone and aqueous solution of NaOH (0.5 M) and stirred while cooling in an ice bath. Then methacryloyl chloride (20 mmol) was added dropwise over 10 min followed by removing the ice bath and stirring the reaction at room temperature for 2 h. Then, acetone was removed by rotary evaporation and the pH was adjusted at 2 by adding HCl (6 M). The precipitated solid was isolated using vacuum filtration on a Buchner funnel and washed with 100 mL of dilute HCl (0.01 M). Thereafter, the white solid was dried in vacuum<sup>2</sup>. Yield = 90–95 %. <sup>1</sup>H NMR (400 MHz, DMSO-d<sub>6</sub>, δ): 10.05 (s, 1H), 7.88 (dd, J = 37.1, 8.6 Hz, 4H), 6.76 (s, 1H), 5.83 (s, 1H), 5.56 (s, 1H), 2.25 (s, 6H), 1.94 (s, 3H).

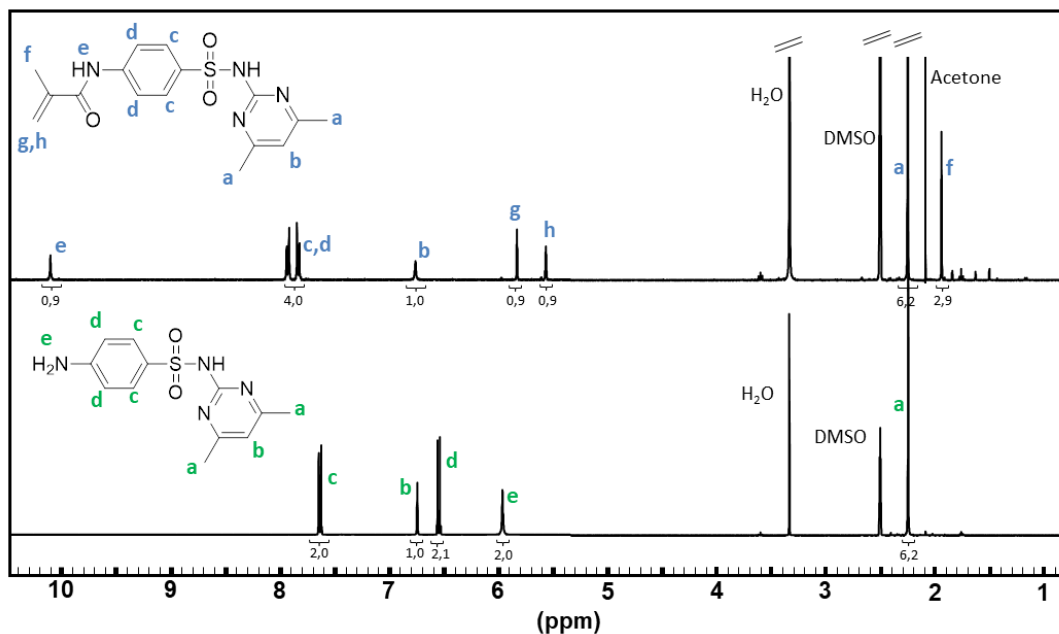


**Figure S5.**  $^1\text{H}$  NMR spectrum (DMSO- $d_6$ , 400 MHz) of SMZ (up) and SZ (down)

**Synthesis of 4-Vinylimidazole (4VIM).** 4VIM was synthesized by decarboxylation of 4-imidazoleacrylic acid under vacuum (1 mbar) at 220-240°C [8]. Yield = 55 %,  $^1\text{H}$  NMR (400 MHz,  $\text{D}_2\text{O}$ ,  $\delta$ ): 7.57 (s, 1H), 6.96 (s, 1H), 6.53 (dd, 1H), 5.53 (dd, 1H), 5.05 (dd, 1H).

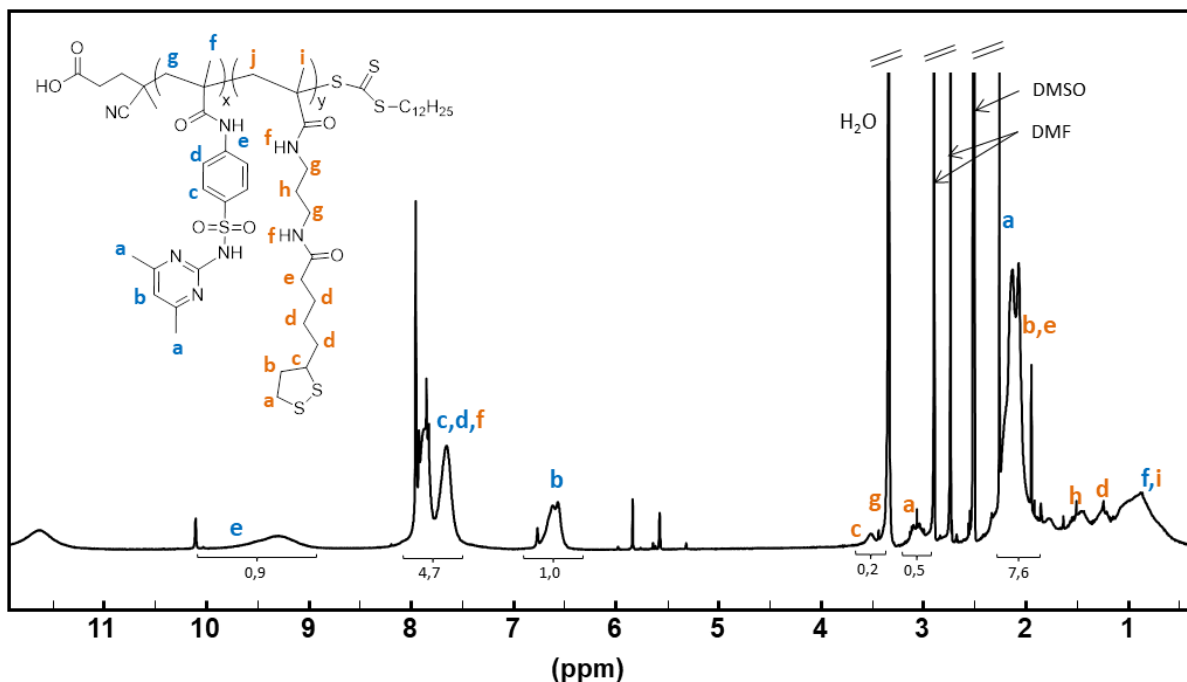


**Figure S6.**  $^1\text{H}$  NMR spectrum (DMSO- $d_6$ , 400 MHz) of  $\text{pSMZ}_{65}/\text{LA}_{15}$

**Synthesis of Sulfobetaine (SB) Methacrylamide macro-CTA.** In the first step, a poly(zwitterion)-macro-CTA was synthesized as described below. 4-cyanopentanoic acid dithiobenzoate (CADB) chain agent transfer (150 mg, 0.54 mmol) was added to a 250 mL round-bottomed flask and dissolved in 2.7 mL of 0.2 M NaOH solution. Immediately after dissolution, 147 ml of sodium acetate buffer solution (120 mM, pH=5.2), 3-[3-methacrylamidopropyl-(dimethyl)-ammonio]propane-1-sulfonate (SB monomer, 16.1 mM), 2,20-azobis(2-amidinopropane) dihydrochloride (V50 initiator, 0.11 mmol, [CADB]/[V50] molar ratio = 5/1) were added. The mixture was purged by argon bubbling for 1 h and thereafter heated in an oil bath at 70°C. After 80 min, the polymerization was quenched by cooling the flask in liquid nitrogen. The polymer was precipitated in acetone, then purified by three cycles of dissolution in water and precipitation in ethanol and finally dried under vacuum. ( $M_n = 6900$  g/mol,  $DP_n = 23$ ,  $M_w/M_n = 1.07$ ). A shorter SB polymer was synthesized by reducing the starting SB monomer/CADB ratio from 60 to 30. ( $M_n = 3400$  g/mol,  $DP_n = 11$ ,  $M_w/M_n = 1.12$ , **Figure S7**).

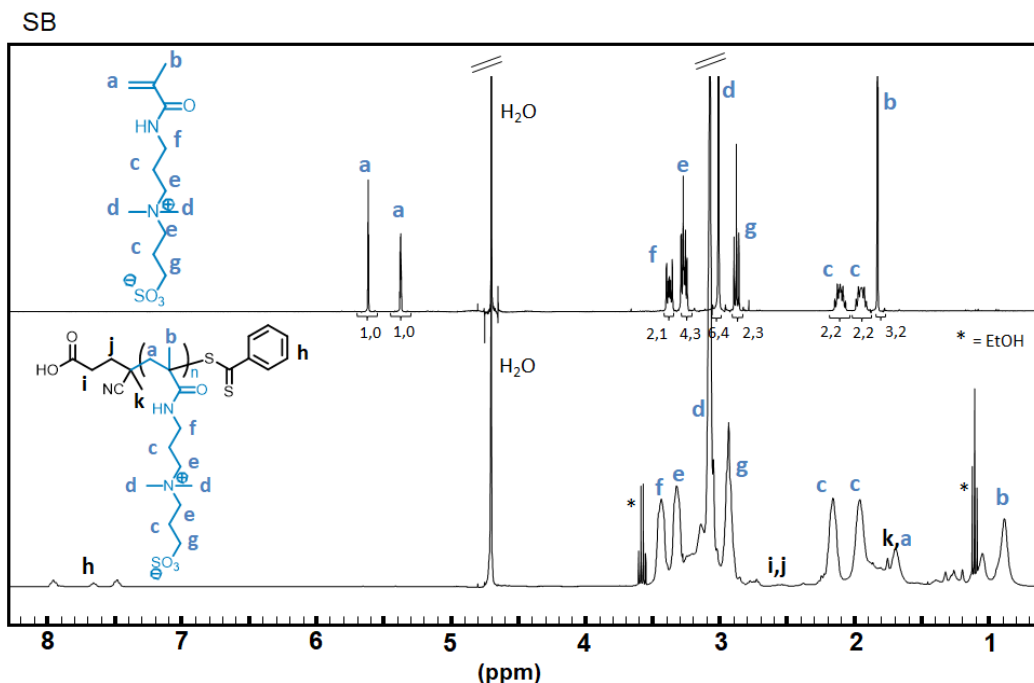


**Figure S7.**  $^1\text{H}$  NMR spectrum ( $\text{D}_2\text{O}$ , 400 MHz) of SB monomer (up) and SB first zwitterionic block (down).

**Poly(SB-*b*-VIM) Synthesis:** The zwitterionic polymer was used as macro raft agent to add a terminal poly(vinylimidazole) block (degree of polymerization of about 10). Typically, SB block ( $M_n = 6900$  g/mol,  $\text{DP}_n = 23$ , 0.39 mmol), 4VIM (0.39 mmol) and 2,2'-Azobis(2-methylpropanitrile) (AIBN, 0.39 mmol) were dissolved in 37 ml of acetic acid containing 10 vol.% of NaCl 100 mM aqueous solution. After degassing with argon, the reaction medium was heated at  $70^\circ\text{C}$  during 6 hours. The crude block copolymer was purified by three cycles of precipitation in ethanol and redispersion in water and finally drying under vacuum. To remove phenyl end groups, the obtained pink-colored block copolymer (500 mg) was dissolved in water (5 mL) and reacted with  $\text{NaBH}_4$  (~50 mg). After 6 h (when the solution turned colorless), the polymer was purified by two cycles of precipitation in acetone and redispersion in water, then precipitated in methanol. The obtained white polymer with a thiol end group was finally dried before use (**Figure S9, S10**). Quantitative  $^1\text{H}$  NMR of crude samples before and after polymerization indicated that about 90 mol % of the vinylimidazole monomers were incorporated into the final product.

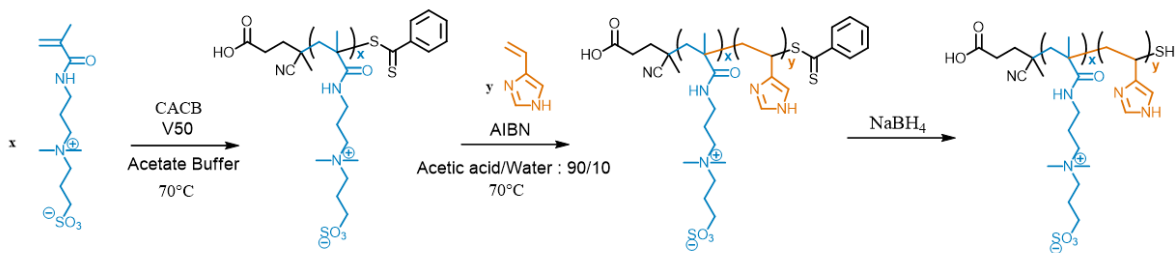


**Figure S8.** Synthesis steps of the SB-*b*-VIM block copolymer.

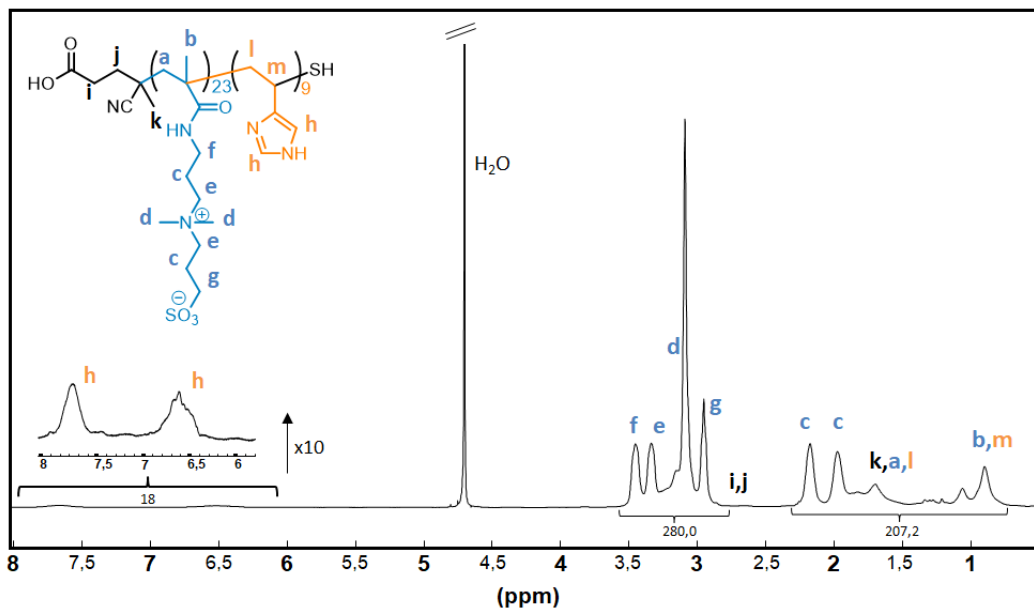


**Figure S9.**  $^1\text{H}$  NMR spectrum ( $\text{D}_2\text{O}$ , 400 MHz) of SB copolymer.

**Synthesis of the short zwitterionic ligand LASB.** A sulfobetaine-appended lipoic acid ligand, LASB, was synthesized following the previously published protocol<sup>3</sup>. Yield = 80 %, <sup>1</sup>H NMR (400 MHz, D<sub>2</sub>O, δ): 3.66-3.75 (m, 4H), 3.46-3.55 (m, 4H), 3.14-3.29 (m, 8H), 2.96-3.01 (t, 2H), 2.44-2.54 (m, 1H), 2.19-2.32 (m, 4H), 1.94-2.05 (m, 1H), 1.55-1.79 (m, 4H), 1.36-1.46 (m, 2H).

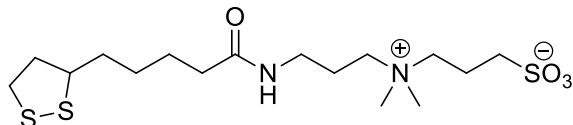


**Figure S10.** Structure of LASB ligand

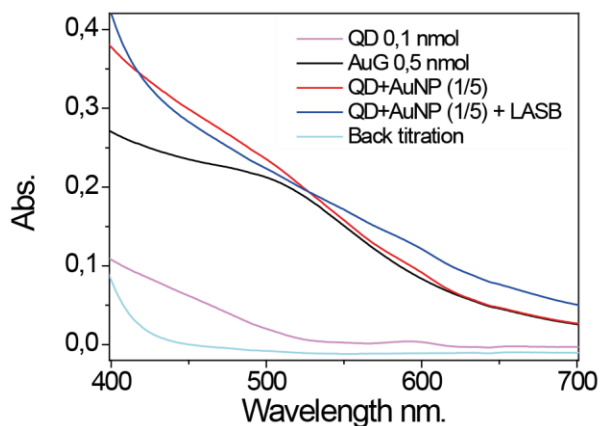


**Figure S11.** Absorbance spectrum of QDs, AuNPs, QD-pSMZ/LA-AuNP assemblies and final filtrate solutions.

**Quantification of the number of gold nanoparticles attached to the QDs.** In order to determine the number of gold nanoparticles attached on each Quantum Dot, a back titration has been performed. After assembling AuNPs onto pSMZ-LA coated QDs and saturation with LASB, the nanoparticle solutions were washed by a series of filtration through a Vivaspin 100 kDa membrane. This step enables elimination of excess LASB and unconjugated AuNPs. Absorbance spectrum of the filtrate solution shows that, under the experimental conditions tested in this work, (AuNP/QD ratio < 0.01), all AuNPs were bound to QD-pSMZ/LA.

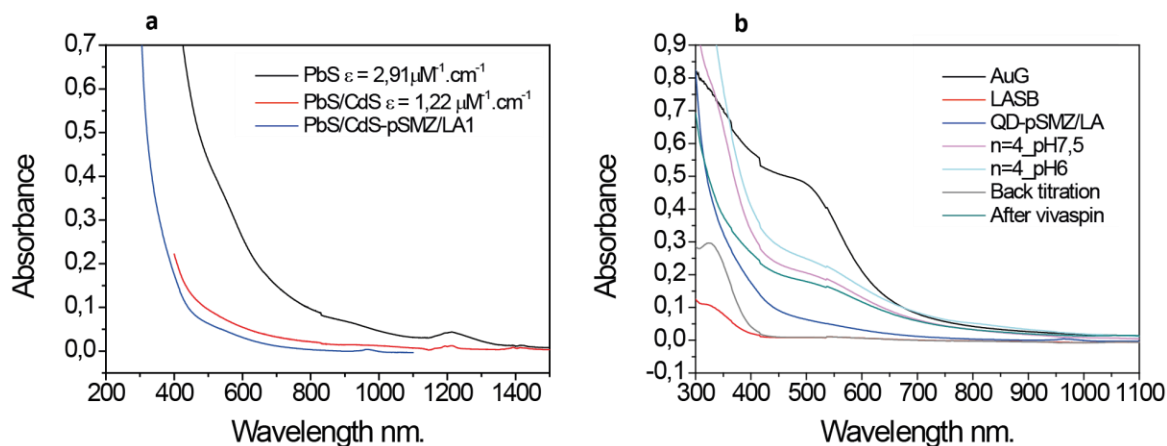


**Figure S12. (A)** Absorbance spectrum of the PbS core, PbS/CdS core-shell and PbS/CdS covered by pSMZ/LA. **(B)** Absorbance spectrum of SWIRQDs, AuNPs, QD-pSMZ/LA-AuNP assemblies and final filtrate solutions.

**Selection of the optimal Au/QD ratio.** Experiments have been realized in order to select the best AuNP/QD ratio to maximize the relative difference in fluorescence intensity between acidic (5.5) and neutral (7.0) pH. Several tubes were prepared with the physiological concentration of NaCl (i.e. 150mM). In each tube 0.05 nmol of QD-pSMZ/LA-AuNP were added with different AuNP/QD ratios of 0, 1, 2, 5, 10, 20 and 50. For each tube, a fluorescence spectrum was realized at pH 7.0 and pH 5.5. The pH was adjusted by NaOH (0.1M) or HCl (0.1M) using a pH-meter. The highest relative fluorescence differences between pH 7.0 and 5.5 occur when for AuNP/QD ratios between 5 and 10.

### Fluorescence spectra and fluorescence lifetime

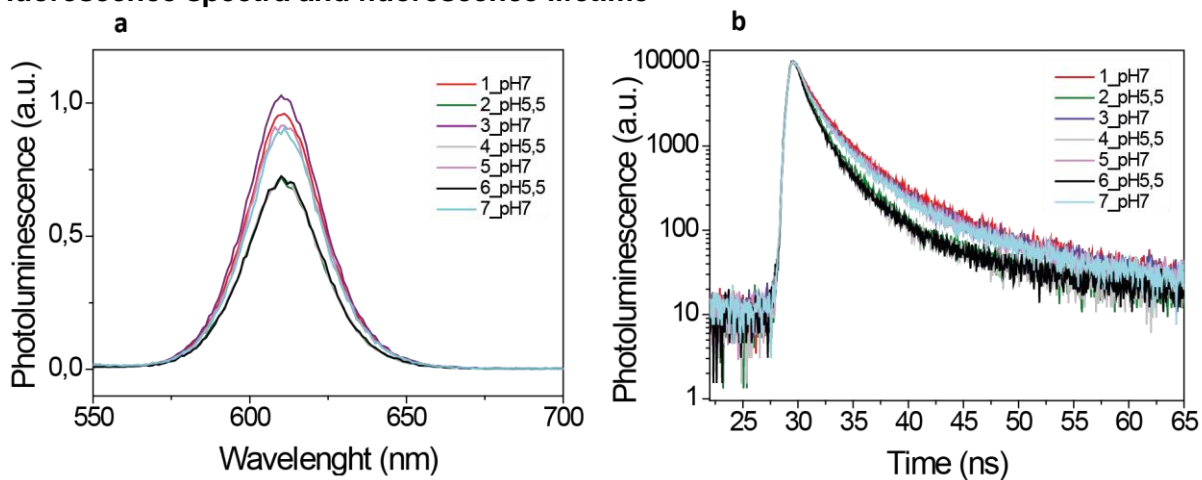


**Figure S13.** (a) Fluorescence spectrum and (b) fluorescence decay of the QD-pSMZ/LA-AuNP corresponding to Figure 4 during 3 cycles of pH variation between 7.0 and 5.5.

## Bi-color sensing at NaCl= 450 mM

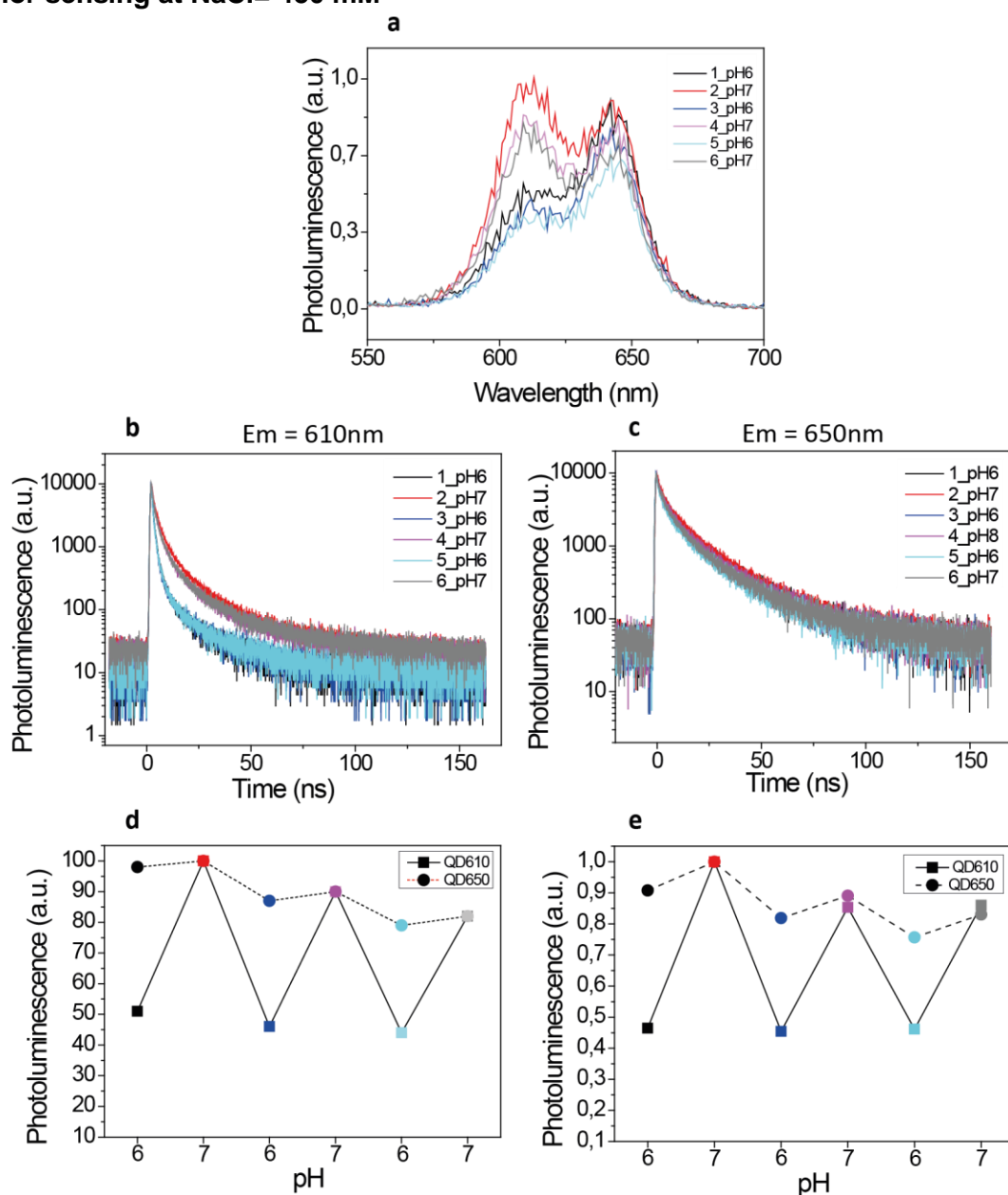


**Figure S14.** Bi-color analyzes with [NaCl] = 450 mM. (a) PL spectrum of QD610-SMZ-Au and QD650-SB over several pH cycling between pH 6 and pH 7. (b) Times-resolved PL with a detector at 610 nm over 3 cycles of pH variations between 6 and 7. (c) Times-resolved PL with a detector at 650 nm over 3 cycles of pH variations between 6 and 7. (d) Ratio between the PL at 610 and 650 nm over the 3 cycles of pH. (e) Ratio between the average PL decay time at 610 and 650 nm over 3 cycles of pH.

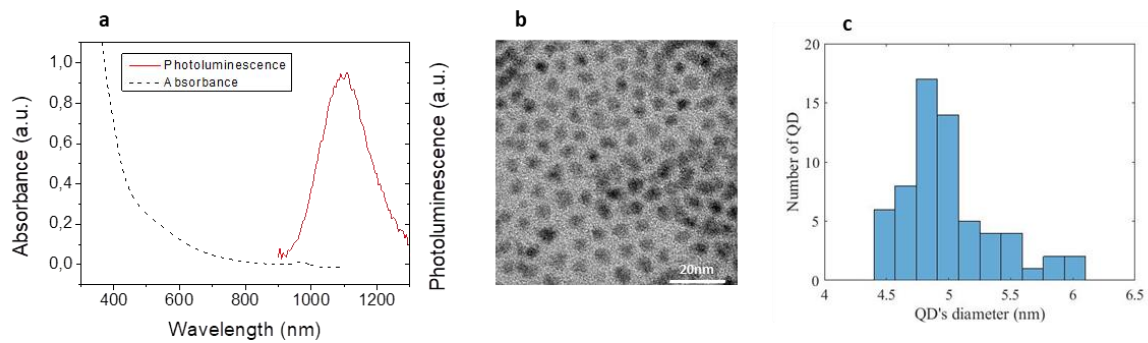


**Figure S15.** (a) Absorption and photoluminescence emission spectra of SWIRQD in water; (b) TEM image of SWIRQD; (c) Size distribution of SWIRQD.

Fluorescence spectrum at NaCl= 150 mM with SWIRQD and reversibility

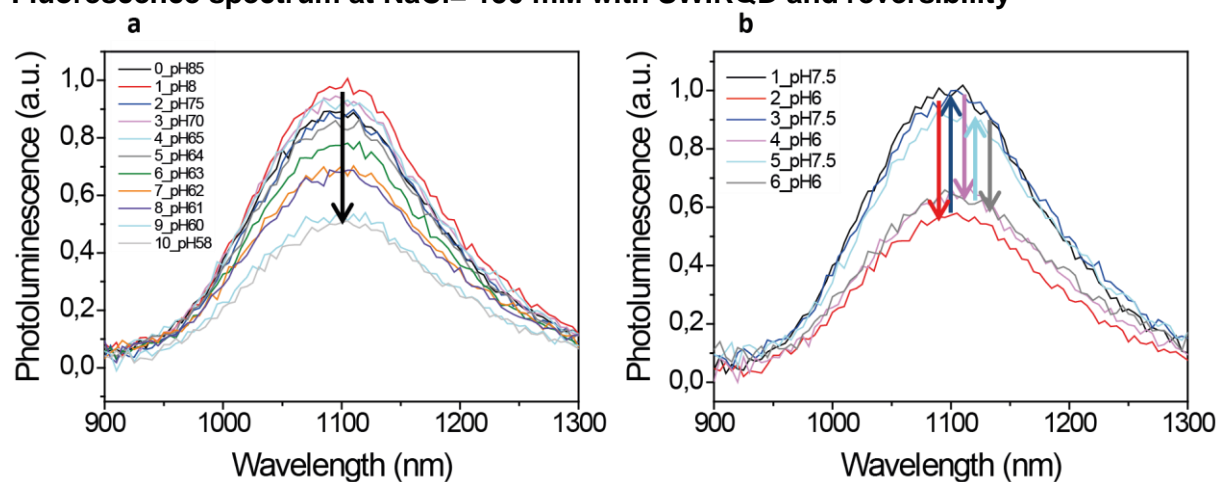


**Figure S16. (a)** Fluorescence spectrum of SWIRQD-pSMZ/LA-AuNP at [NaCl] = 150 mM depending on the pH. **(b)** Three pH variation cycle between 7.5 and 6.

## References

- (1) Giovanelli, E.; Muro, E.; Sitbon, G.; Hanafi, M.; Pons, T.; Dubertret, B.; Lequeux, N. Highly Enhanced Affinity of Multidentate versus Bidentate Zwitterionic Ligands for Long-Term Quantum Dot Bioimaging. *Langmuir* **2012**, *28* (43), 15177–15184.
- (2) Abel, B. A.; Sims, M. B.; McCormick, C. L. Tunable PH- and CO<sub>2</sub>-Responsive Sulfonamide-Containing Polymers by RAFT Polymerization. *Macromolecules* **2015**, *48* (16), 5487–5495.
- (3) Park, J.; Nam, J.; Won, N.; Jin, H.; Jung, S.; Jung, S.; Cho, S. H.; Kim, S. Compact and Stable Quantum Dots with Positive, Negative, or Zwitterionic Surface: Specific Cell Interactions and Non-Specific Adsorptions by the Surface Charges. *Adv. Funct. Mater.* **2011**, *21* (9), 1558–1566.
- (4) Antonelli, A.; Sfara, C.; Battistelli, S.; Canonico, B.; Arcangeletti, M.; Manuali, E.; Salamida, S.; Papa, S.; Magnani, M. New Strategies to Prolong the In Vivo Life Span of Iron-Based Contrast Agents for MRI. *PLoS One* **2013**, *8* (10), 1–17.
- (5) Deuticke, B.; Kim, M.; Zöllner, C. The Influence of Amphotericin B on the Permeability of Mammalian Erythrocytes to Nonelectrolytes, Anions and Cations. *BBA - Biomembr.* **1973**, *318* (3), 345–359.